An infrared thermography study on the thermal load experienced by a high power Hall thruster

IEPC-2005-63

S. Mazouffre[*], J. Pérez Luna[†], D. Gawron[‡], M.Dudeck[§]
Laboratoire d'Aérothermique, CNRS, 1C Avenue de la Recherche Scientifique, Orléans, 45071, France

P. Echegut[**]
CRMHT, CNRS, 1C Avenue de la Recherche Scientifique, Orléans, 45071, France

Abstract: The thermal behavior of a high power PPSX000 Hall effect thruster was investigated by means of calibrated infrared imaging over a broad range of input power. The steady state dielectric channel wall temperature varies roughly as the square root of the applied power meaning that the temperature depends neither upon the current-voltage pair nor upon the magnetic optimization. A semi-empirical time-dependent thermal model of a Hall thruster was developed to calculate changes in time of the thruster channel temperature during a transient regime. The model accounts for heat conduction through dielectric walls and radiative transfer between surfaces. The grey body viewing factors are experimentally determined during thruster shutdown stages. The calculated temperature profiles are fitted to experimental ones in order to extract the energy flux deposited by the plasma onto a given surface element. Surprisingly the energy flux varies linearly with the applied power whatever the current-voltage couple. Such a simple evolution law seems in contradiction with the complexity of plasma dynamics at work in a Hall thruster. For the PPSX000 thruster about 7 % of the applied electric power is lost onto the dielectric channel walls that corresponds to several kW per unit area. The energy deposition mechanisms are still unknown, however, interactions between charged particles and walls certainly play a key role, as does the structure and properties of the plasma sheath.

Nomenclature

α = thermal diffusivity, $m^2\,s^{-1}$
c_p = specific heat, $J\,kg^{-1}\,K^{-1}$
ε = normal spectral emissivity
ϕ = energy rate per unit area, $W\,m^{-2}$
G = grey body view factor
h = dielectric wall thickness
I_d = discharge current, A
κ = thermal conductivity, $W\,m^{-1}\,K^{-1}$

---

[*] Research scientist, CNRS.
[†] Graduated student, ENSICA.
[‡] PhD student, CNRS.
[§] Prof., University of Paris VI.
[**] Research scientist, CNRS.

λ	=	wavelength, m
P	=	applied electrical power, W
q_p	=	energy flux deposited by the plasma onto a surface, W m^{-2}
ρ	=	density, kg m^{-3}
t	=	time, s
T	=	temperature, K
S	=	surface, m^2
U_d	=	discharge voltage, V
σ	=	Stefan-Boltzmann constant ($\sigma = 5.6704 \times 10^{-8}$ W m^{-2} K^{-4})
r, z, θ	=	radial, axial, azimuthal directions, respectively

Subscripts

ext	=	outer channel dielectric wall
int	=	inner channel dielectric wall
p	=	plasma
rad	=	radiative flux

I.   Introduction

The Hall effect thruster (HET) thermal state during operation determines to a large extent the discharge chamber wall properties such as secondary electron production and erosion rate, as well as anode properties like sputtering yield. The thruster temperature also determines outgassing speed into vacuum when tests are conducted in ground-based facility. Therefore, the temperature field greatly influences HET performances and efficiency by acting onto discharge current and thrust. Thermal stress endured by a HET during ignition and shut down stages and overall thermal load experienced during firing certainly influence the thruster lifetime. Finally, accurate knowledge about thermal load undergone by a HET is of great relevance for radiator design purposes, lifetime prediction, and running cycle definition. Therefore, the acquisition of reliable data about temperature of HET elements such as discharge chamber thermal insulators, metal body, coil or magnet housing, hollow cathode body is crucial for existing thruster optimization and development of a versatile high power HETs.

In most of experimental works dedicated to thermal characterization of Hall effect thrusters, the temperature of various thruster components was determined by means of thermocouples[1]. Thermocouples embedded in the thruster structure provide a standard means of temperature determination, however, severe plasma conditions encountered in HET discharge chamber as well as access restriction greatly complicate the measurement process. Another way to estimate temperature fields in a HET consists in employing a radiative-conductive thermal model[2]. However, such a method relies on estimations of the overall HET energy balance that is still lacking of accuracy.

Thermal imaging is first a qualitative diagnostic technique that permits to obtain relative temperature change during thruster thermal cycles as well as when varying working parameters. Nevertheless, the present state of commercially available technology makes infrared imaging a quantitative diagnostic provided that the emissivity of the viewed area is known. Nowadays, calibrated infrared camera can provide absolute temperature with a good accuracy at each pixel element. Thermal imaging has been applied to acquire infrared images of gridded ion engines[3]. In a previous contribution, we presented first results that concerned the determination of Hall effect thruster temperature field by means of infrared thermography[4]. The thermal behavior of a SPT-100 laboratory model thruster in various configurations was investigated as well as the thermal behavior of a PPS®1350-G thruster[††] under standard operating conditions and in high input power regimes. In the present contribution we present results that concern infrared thermography measurements of the thermal load experienced by a PPSX000 thruster[5]. This thruster is a high power Hall effect thruster with dual mode capability that can be operated either in high specific impulse mode or in a high thrust regime. The temperature field of inner and outer dielectric channel walls, of the ceramic back wall of the channel as well as of the anode, which also serves as gas injector, was measured as a function of time for various applied power. The influence of both the applied voltage and the supplied gas mass flow upon the steady state thruster component temperature is discussed. A semi-empirical thermal model of the thruster

---

[††] The PPS®1350-G thruster, which is developed by Snecma, equips the SMART-1 lunar space probe from the European Space Agency.

The 29th International Electric Propulsion Conference, Princeton University,
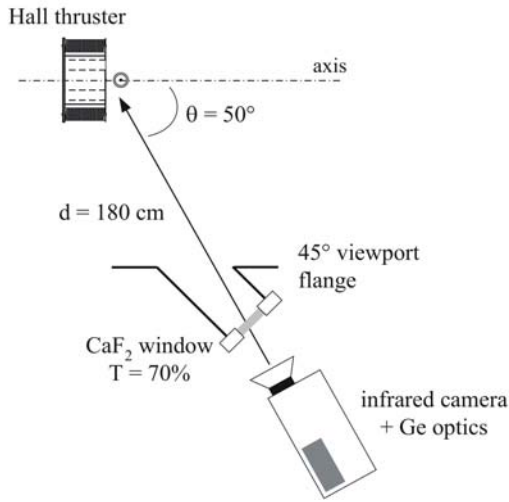*October 31 – November 4, 2005*

Figure 1. Schematic drawing of the experimental arrangement used for IR thermal imaging of Hall thrusters in the PIVOINE ground-test facility.
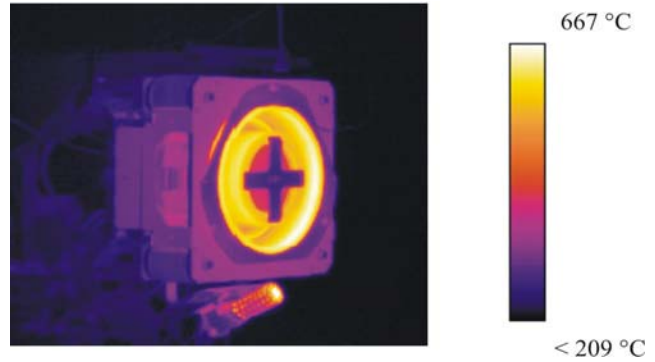

Figure 2. Calibrated infrared image of the PPSX000 Hall effect thruster operating at 4.5 kW input power. The inner and outer thermal insulator temperature is 598°C and 622°C, respectively ($\varepsilon = 0.92$).

channel as been developed in order to be able to calculate the time evolution of the wall temperature. When fitting the model outcomes to measured time-resolved temperature profiles, it is possible to determine with a great accuracy the energy flux deposited by the plasma onto the discharge chamber walls. This quantity allows to better understand energy losses mechanisms at work inside the channel and to refine the overall power balance of a HET. Furthermore a large data set is readily useful for a direct comparison with thermal models of high power Hall effect thrusters.

II. Experimental arrangement and thermograms

Infrared thermal imaging is based on the Planck's radiation law that relates the number of photons per unit volume per unit wavelength-interval emitted by a black body, i.e. a perfect radiator, to the temperature of the latter[6]. Since infrared detectors are solely able to capture radiations in a narrow wavelength band $\Delta\lambda$, the Planck's law must be integrated over $\Delta\lambda$ to obtain the body surface temperature. The overall power $\Phi_{\rm rad}$ radiated into a hemisphere by a blackbody is obtained from integration of the Planck's law over the entire spectral domain. It leads to the well-known Stefan-Boltzmann's relation, which reads for a grey body:

$$\phi_{\rm rad} = \varepsilon(T)\,\sigma\,T^4 \,. \tag{1}$$

The Hall thruster infrared image acquisition has been accomplished with a computer controlled calibrated infrared camera ThermaCAM**TM**SC 3000 manufactured by FLIR systems[7]. The infrared camera is equipped with a GaAs Quantum Well Infrared Photodetector that consists of a set of 320×240 pixels. The QWIP is Stirling-cooled down to -200 °C to reduce the camera intrinsic noise. The detector is suited for the 8-9 μm spectral domain. An overall temperature range from -20 °C to 2000 °C is covered by automatically adjusting an internal shutter. A camera frame rate up to 750 Hz is available, which allows to perform time-resolved infrared measurements in view of the long thermal time scale. The majority of images were acquired with a frame rate of 50 Hz.

All experiments were conducted in the PIVOINE test chamber. A sketch of the experimental arrangement is depicted in Fig. 1. The infrared camera was located at a distance of 180~cm from the HET front plate. The thruster observation angle was 60°, in which case the camera viewed virtually the entire thruster. Observation was carried out through a 10~mm in thickness CaF$_2$ window with a 70 % transition in the 8-9 μm IR band. The transmission coefficient was measured with a FTIR spectrometer. In order to improve the image resolution of thruster components, magnified images were produced with the use of Ge optics with 10° and 7° numerical aperture in
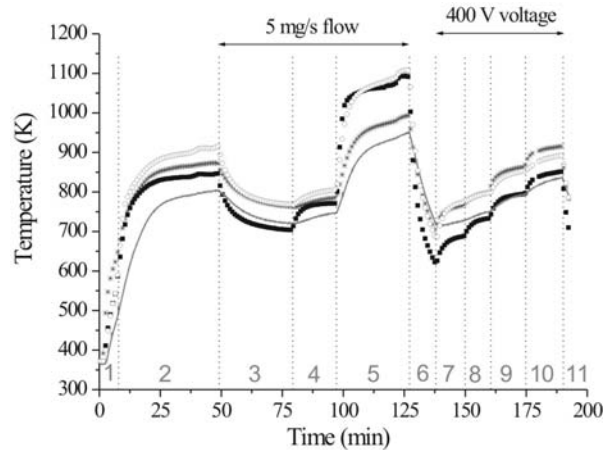
Figure 3. Mean temperature of various elements of the PPSX000 thruster as a function of time when varying the applied power : Anode (asterix), outer wall (square), inner wall (circle) and bottom (line). Sequences 6 and 11 correspond to a shutdown stage. During this measurement series the thruster was equipped with a graphite anode.
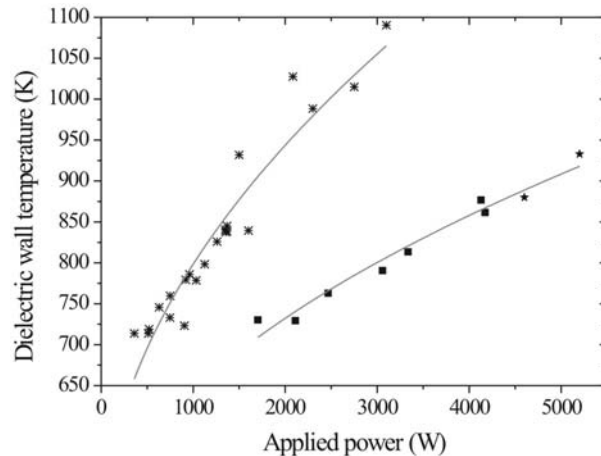
Figure 4. Average temperature of BN-SiO$_2$ dielectric walls of two thrusters as a function of applied power ($I_d \times U_d$): SPT100-ML (asterix), PPSX000 with a graphite anode (square) and with a stainless steel anode (star). The solid lines correspond to a power law fitted to the two data sets. In the two cases the exponent is 0.5.

horizontal and vertical direction, respectively. Note that additional optics are automatically recognized by the camera and the ad hoc correction is subsequently performed.

In order to enable absolute temperature determination for the thruster discharge chamber dielectric walls, the spectral emissivity of a fresh BN-SiO$_2$ ceramic piece manufactured by SINTEC has been measured for several temperatures. The measurements were performed with a Fast Fourier Transform spectrometer Bruker IFS 113v improved to work in emission configuration over a large spectral range an a wide temperature domain. The emissivity does not change much with temperature[4] : In the 8-9 μm spectral band probed by the infrared camera, the BN-SiO$_2$ emissivity mean value is 0.92. The emissivity of a given sample depends upon wavelength and temperature as previously mentioned, but also upon viewing angle, material composition, and surface conditions like roughness and oxidation level. Within the 8-9 μm spectral interval probed by the infrared camera one can consider that the emissive response of the BN-SiO$_2$ dielectric sample is almost that of a grey radiator. Furthermore, a ceramic can be assumed to obey Lambert's law to a large extent. The emissivity of a given element can vary in the course of thruster operation owing to wear, change in geometry, and coating formation. Performing infrared imaging under fixed thruster working conditions but with ceramic walls having a different history we found that the BN-SiO$_2$ emissivity stays unchanged. The anode of the PPSX000 thruster is made of either stainless steel or graphite. In order to obtain an estimate of the anode temperature, the emissivity of the latter was fixed to 0.8 whatever the material.

A calibrated infrared image of a PPSX000 Hall effect thruster taken with the infrared camera while operating at 5 kW is shown in Fig. 2. The emissivity is fixed to 0.92, i.e. the temperature field is solely correct for the discharge chamber ceramic walls. The PPSX000 thuster dimensions are greater than the one of the SPT100 to achieve proper plasma conditions at high power. The thickness of both inner and outer dielectric wall is a few mm. In Fig. 2 one can easily distinguished the thruster body, the coil housings, the internal pole, the discharge chamber wall that act as thermal insulators, the hollow cathode body as well as a small fraction of the anode. In the left part of Fig. 2, the thruster holder and a set of electrical cables are also visible. The inner and outer walls, which sustained the power dissipated by the plasma, together with the anode/gas distributor, which collects the discharge current, are clearly the most intense infrared source in the image.

III. Steady state dielectric wall temperature

The PPSX000 thruster temperature field has been monitored for a large set of operating conditions ranging from 1.6 kW to 5.2 kW applied power. An example of measurement sequence is displayed in Fig. 3 for a PPSX000 equipped with a graphite anode. Stages labeled 6 and 11 correspond to a power shut-down. Note that the thruster is always magnetically optimized when changing the operation conditions, i.e. the magnetic field is modified by varying the current flowing through all solenoids in order to minimize the discharge current. The temperature values indicated in Fig. 3 correspond to values averaged over the entire surface of the concerned element. Nevertheless, the wall temperature is relatively homogeneous. Along the axial direction z, the temperature gradient can however reach up to 100 K. For the inner and outer walls, the area of highest temperature is always located near the exit of the thruster channel meaning that most of the energy is lost by the plasma within the ion acceleration layer. Along the azimuthal direction θ, the temperature gradient is below 50 K even at high applied power.

In Fig. 4, the average temperature of BN-SiO$_2$ ceramic walls T_{wall} is plotted as a function of the applied power for the SPT100-ML thruster and for the PPSX000 thruster. The average wall temperature is given by:

$$T_{\text{wall}} = \tfrac{1}{2}\left(T_{\text{ext}} + T_{\text{int}}\right),\tag{2}$$

where T_{ext} is the outer (external) dielectric wall temperature and T_{in} is the inner (internal) wall temperature. The two measured temperatures correspond to the mean surface temperature in the final section of the channel ($\Delta z \approx 20$ mm) where most of the energy is lost. First, for a given supplied power, T_{wall} is much less for a PPSX000 HET that reveals the good thermal design of this high power thruster[5]. Radiators with optimized architecture have been added to the thruster. The thruster body and magnetic circuit are open to enable the outer dielectric wall to evacuate most of its thermal power outwards without heating too much its surroundings. In such a way the amount of power stored in secondary heat sources like metal elements and coils is limited. Moreover, the low T_{wall} for a PPSX000 thruster in comparison with a SPT100 thruster also originates from the fact the surface to volume ratio $\mathfrak{R}$ is higher for the former, which allows a better power losses distribution:

$$\frac{\mathfrak{R}_{\text{PPSX000}}}{\mathfrak{R}_{\text{SPT100}}} = 2.1\,.\tag{3}$$

Assuming that T_{wall} keep following the trend observed in Fig. 4 at high power, the mean wall temperature would reach 1100 K at 10 kW applied power, much below the BN-SiO$_2$ ceramic maximum sustainable temperature. Second, for the two thusters, the wall temperature varies as the square root of the input power. In Fig. 4, a power law is fitted to the two data sets fixing the exponent to 0.5. The following variation laws are then obtained:

$$\text{SPT100:} \quad T_{\text{wall}} = 447 + 11.1 \times P^{0.5}\tag{4}$$
$$\text{PPSX000:} \quad T_{\text{wall}} = 429 + 6.8 \times P^{0.5}\tag{5}$$

In Eq. (4) and (5) the constant corresponds to the temperature of a thruster at rest. In a ground-test facility this temperature is closed to 300 K. The gap between calculated and real values suggests that the behavior of T_{wall} may be different at low input power ($P < 500$ W). Whatever the exact form of the dielectric wall mean temperature variation law with applied power, experimental curves displayed in Fig. 4 reveal interesting features. T_{wall} is solely a function of the input power $P = I_d \times U_d$: In other words for a given power level it does not depends upon the current-voltage pair[8]. Such a simple trend is clearly in contradiction with the complexity of the plasma dynamics at work in a Hall effect thruster[9,10]. In a first order approximation, increasing the discharge current, i.e. the injected propellant mass flow rate, leads to an increase in the charged particles density. On the contrary, increasing the discharge voltage leads to an increase in the particles kinetic energy inside the channel. A different thermal behavior is then expected when changing the two quantities. One way to solve the apparent contradiction is to consider that processes occurring within the plasma sheath, e.g. saturation, are at the origin of this unexpected trend. One may also consider the role of UV radiations. The question is still open and it certainly needs further investigation. Moreover, T_{wall} does not depend upon the magnetic field if changes are not too important. In Fig. 4, all points have been optimized for the PPSX000 thruster and most of the points were optimized in the case of the SPT100-ML[8]. Finally, the same variation law, i.e. $T \propto P^{0.5}$, is obtained for various materials and for a given material the law does not depends on the thruster history[8].
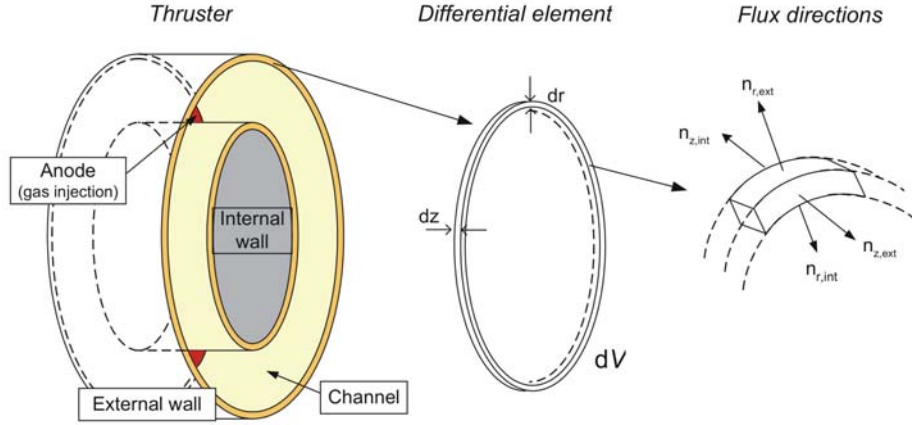
Figure 5. Simplified drawing of a HET channel and differential elements considered in our model for the energy conservation equation.

IV. Time-dependent thermal model of a HET

A. Energy conservation equation

The time-dependent thermal model we developed for a Hall effect thruster is naturally based on the energy conservation equation. Consequently, we will first write this equation for a differential element of the discharge channel wall. As previously discussed, the channel wall temperature does not vary much with the azimuthal angle θ. Therefore, the first assumption is to consider the problem as axisymmetric. The differential element of interest is then the elementary ring shown in Fig. 5. The same equation will of course apply for an element of the outer wall and for an element of the inner wall. However, as we will see, boundary conditions for the two elements will differ. Let T be the temperature of the elementary volume dV, E its energy, ρ its density and ϕ_i the outgoing energy rates through the corresponding surfaces dS_i. The energy equation for the control volume dV reads:

$$\rho \frac{dE}{dt} dV = -\sum_i \vec{\phi}_i \cdot \vec{n}_i \, dS_i \, . \tag{6}$$

The considered volume being motionless, the energy reduces to the enthalpy: $dE = dH = \rho \, c_p \, dT$. After developing the sum, the energy conservation equation writes:

$$\rho c_p \frac{\partial T}{\partial t} dV = -\vec{\phi}_{r,ext} \cdot \vec{n}_{r,ext} dS_{r,ext} - \vec{\phi}_{r,int} \cdot \vec{n}_{r,int} dS_{r,int} - \vec{\phi}_{z,ext} \cdot \vec{n}_{z,ext} dS_z - \vec{\phi}_{z,int} \cdot \vec{n}_{z,int} dS_z \, . \tag{7}$$

The walls' thickness h is small in comparison with the inner and outer channel wall radii. We can therefore consider that $dS_{r,ext} \approx dS_{r,int} = dS_r$. Previous equation becomes:

$$\rho c_p \frac{\partial T}{\partial t} dV = -\left(\vec{\phi}_{r,ext} \cdot \vec{n}_{r,ext} + \vec{\phi}_{r,int} \cdot \vec{n}_{r,int} \right) dS_r - \left(\vec{\phi}_{z,ext} \cdot \vec{n}_{z,ext} + \vec{\phi}_{z,int} \cdot \vec{n}_{z,int} \right) dS_z \, . \tag{8}$$

At that point we must list the different heat rates involved in the study of energy transfers inside the channel of a Hall effect thruster and discuss their respective magnitude:

a) The only possible heat flux along the z axis is the conductive heat flux: $\phi_z(r,z) = -\kappa \frac{\partial T}{\partial z}$. However, at high temperature and in the case of a BN-SiO$_2$ dielectric wall, the amount of power transferred in the z direction can be neglected compared with the radiative power[11].
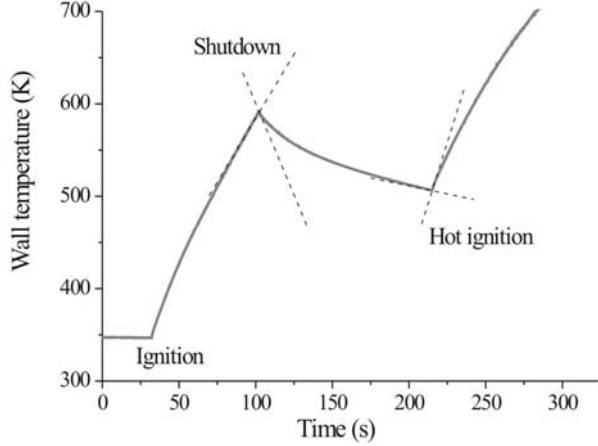
6

Figure 6. Principle of the "go and stop" approach: q_p can be determined at thruster shutdown and hot ignition in a simple way by calculating the tangent. Temperature profile of a SPT100 HET under standard operation conditions.
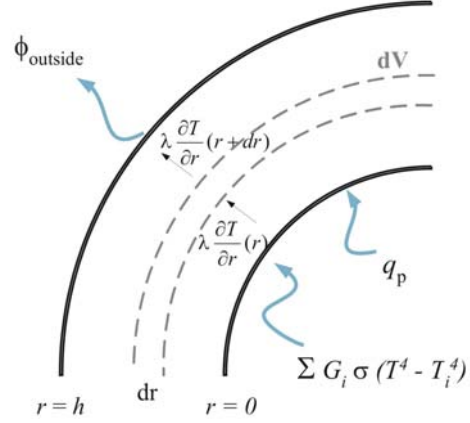
Figure 7. Energy balance for the outer dielectric wall used in the semi-empirical time-dependent thermal model. On the contrary, the inner wall is assumed to be adiabatic and $\phi_{ouside} = 0$.

b) In radial direction, one must distinguish between two kinds of elements:

- for a bulk element, a conductive heat flux is considered: $\phi_r(r,z) = -\kappa \dfrac{\partial T}{\partial r}$,

- for a boundary element, heat is exchanged thanks to radiative processes: $\phi_{rad}(z) = \sum_i G_i \sigma (T^4 - T_i^4)$, where T is the element surface temperature, T_i is the temperature of the surface i facing the considered element and G_i the grey body view factor between the element and the environment element i.

c) Hall thrusters operating in a low pressure medium, convective flux is neglected,

d) The energy flux deposited by the plasma onto a surface element $q_p(z)$. The magnitude of q_p will be inferred from direct comparison between numerical outcomes and experimental data.

Finally, neglecting convective effects as well as axial heat conduction the energy conservation equation for a HET channel wall element reads:

$$\rho c_p \frac{\partial T}{\partial t} dr = -\left(\vec{\phi}_{r,ext} . \vec{n}_{r,ext} + \vec{\phi}_{r,int} . \vec{n}_{r,int} \right). \tag{9}$$

In the next sections we describe two approaches to solve Eq. 9 for all walls of the channel and we propose a way to experimentally determine the view factors.

B. The "go and stop" approach

   At thruster ignition, heat conduction dominates energy exchange processes in view of the low channel temperature. The energy conservation equation then reduces to Fourier's law of heat conduction and the channel wall can be considered as an infinitely thick plane plate[4]. However, this very simple model is solely valid for short time period in the order of 10 s since the relation $h < \sqrt{\alpha t}$ must be valid. At thruster ignition, due to outgassing phenomena the discharge current varies in time meaning that plasma properties are not stationary, especially q_p, and the Fourier's law cannot be solved. Therefore in most cases this model cannot be used right after ignition. This rough model assumes the wall can store an infinite amount of energy. As a consequence, when applying this approach for a long time period $\Delta t > h^2/\alpha$ during which q_p does not change, the value of q_p obtained from a comparison between calculations and measurements is overestimated.

   Instead of considering a wall of infinite thickness, a better assumption is to consider that the temperature gradient through the wall is always zero. This assumption seems reasonable in view of the low ceramic wall thickness ($h = 4.5$ mm). Let us now consider heat transport mechanism during a very short period of time. At high
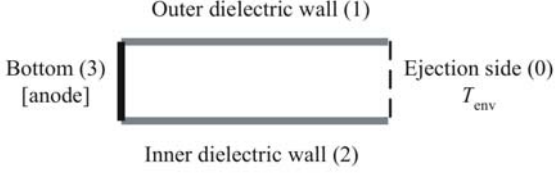
Figure 8. Radiative enclosure used to calculate the view factor.

temperatures, the radiation characteristic time scale is far smaller than the conduction characteristic time scale[11]. Heat conduction can then be neglected. Under this assumption, the energy conservation equation reads:

$$\rho\, c_p\, \frac{dT}{dt} h = -\sum_i G_i\, \sigma\, (T^4 - T_i^4) + q_p + \phi_{\text{outside}}, \quad (10)$$

where ϕ_{outside} stands for the energy evacuated by the outer side of the external wall. This term only appears in the equation that concerns the external wall. Indeed the internal ceramic wall does not evacuate power through its inner side since it radiates on itself (the existence of a magnetic coil is neglected in this picture). Equation 10 allows to extract the value of q_p in an elegant manner when considering either a thruster shutdown stage or a hot ignition stage (starting from a warm thruster) far from thermal equilibrium, as shown in Fig. 6. In the two cases, we will compare the thermal behavior with a plasma (thruster on) and without a plasma (thruster off). The energy conservation equation reads respectively before and after shutdown at t_0:

- $t = t_0^-$
$$\rho\, c_p\, \frac{dT}{dt} h = -\sum_i G_i\, \sigma\, (T^4 - T_i^4) + q_p + \phi_{\text{outside}} \quad (11)$$

- $t = t_0^+$
$$\rho\, c_p\, \frac{dT}{dt} h = -\sum_i G_i\, \sigma\, (T^4 - T_i^4) + \phi_{\text{outside}} \quad (12)$$

Preceding equations are written down for the external channel wall. For the internal wall, the term ϕ_{outside} must be withdrawn. The temperature of each element (T_i and T) is a continuous function, therefore: $T(t_0^-) = T(t_0^+)$. The grey body view factors G_i depend only on the geometry and on the radiative properties of the ceramic, so they are the same before and after t_0 as long as ε does not change. Substracting Eq. 12 from Eq. 11, one finds:

$$q_p = \rho\, c_p\, h\left(\left|\frac{dT}{dt}\right|_{0^-} - \left|\frac{dT}{dt}\right|_{0^+} \right). \quad (13)$$

Thus the energy flux deposited by the plasma onto a wall is given by the slope difference before and after the shutdown. The same technique applies for a hot ignition stage, however, Eq. 13 must be inverted. This method, the so-called "go and stop" approach, is useful to have an estimate of q_p because it is very simple and perfectly adapted to the infrared imaging technique. Moreover this approach can be applied to any operating conditions. Nevertheless, the "go and stop" approach has some drawbacks. First, shutdown and ignition of the thruster can create phenomena like outgassing that are not taken into account. Second, the slopes can only be determined with a good accuracy if a high temporal resolution is set, which necessitates a high data storage capacity. Nevertheless, under identical thruster operation conditions the slopes are found to slightly vary from a measurement to another. Third, this method requires a dedicated operation on the thruster, i.e. shutdown or ignition. For all these reasons, it is interesting to

	11	12	13	10	22	21	23	20
Theoretical F	0.06	0.611	0.444	0.444	0	0.434	0.232	0.232
Theoretical G	0.192	0.541	0.345	0.406	0	0.408	0.213	0.222
Fitted G	0.2	0.5	0.35	0.3	0	0.45	0.2	0.2

Table 1. Theoretical view factor F and grey body view factor G for the outer (1) and inner (2) ceramic walls of the PPSX000 thruster. The fitted G factors are obtained from measured temperature evolution during a thruster shutdown stage.
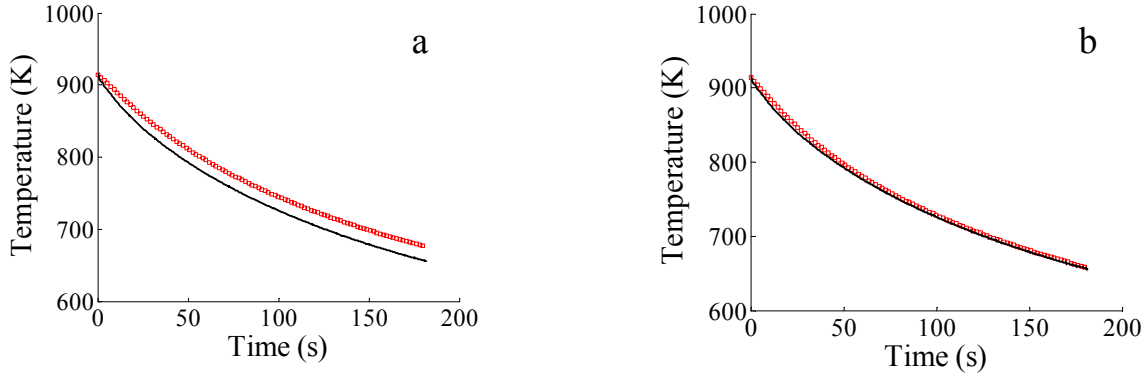
Figure 9. Mean outer channel wall temperature as a function of time after a shutdown of the PPSX000 thruster. a) Comparison between experimental data (solid line) and numerical outcomes (square) using the theoretical grey body view factors *G*. b) The calculated curve is fitted to the measured one by playing with the *G* factor values. The obtained set of fitted G factors is then used in the model to perform thermal behavior simulations.

develop a more elaborated thruster thermal model which could permit to estimate q_p at any moment without modifying thruster working parameters.

C. The semi-empirical time-dependent thermal model

Even if the "go and stop" approach is attractive, it solely provides us with an estimate of q_p. The need for a more elaborated thermal model of a HET channel is then obvious. In this section we build up a model able to furnish with a channel wall element temperature at any time without disturbing the thruster working regime. Our thermal model is based on the following assumptions:

- the energy flux q_p is not time-dependent (stationary plasma properties),
- conduction along the z and θ directions is neglected,
- the environment is at low-pressure and it exhibits a fixed temperature T_{env},
- the external wall radiates part of its energy outwards,
- the internal wall loses no energy through its inner side (adiabatic wall),
- the thermodynamic parameters (ε, κ, c_p, ρ) do not depend upon the temperature.

Therefore, the remaining energy rates involved in our study are:

   - a conductive heat flux through the wall,

   - a radiative flux for all surfaces,

   - the energy deposited by the plasma q_p which is the unknown variable,

   - for the external side of the outer dielectric wall, a thermal radiation heat flux towards the outside $\phi_{outside}$.

The drawing in Fig. 7 indicates all energy fluxes taken into account in the model. With this set of assumptions, the energy conservation equation reduces to the well-known unsteady heat-conduction equation with no sources or sinks:

$$\frac{\partial T(r,t)}{\partial t} = \alpha \frac{\partial^2 T(r,t)}{\partial r^2} . \tag{14}$$

The appropriate boundary conditions are (see Fig. 7):

$$\lambda \left[\frac{\partial T}{\partial r} \right]_{r=0} = \sum_i G_i \, \sigma \, (T^4 - T_i^4) + q_p \quad \text{for both the inner and outer dielectric walls,}$$
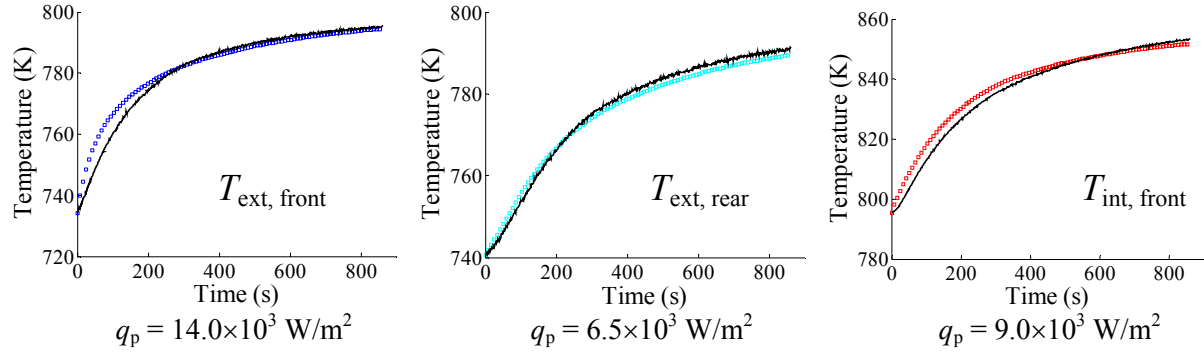
Figure 10. Evolution in time of the channel wall temperature for a PPSX000 thruster operating at 3.2 kW: thermal imaging data (line) and numerical outcome using fitted G factors (square). Also shown is the power deposited by the plasma onto the dielectric walls. Two parts are considered: The rear half and the front half.

$$\lambda \left[\frac{\partial T}{\partial r} \right]_{r=h} = \phi_{outside} \text{ for the outer wall,}$$

$$= 0 \text{ for the inner wall.}$$

With such complicated boundary conditions, Eq. 14 cannot be solved analytically and one must turn towards a numerical approach. We used a finite element method to solve Eq. 14 for the thruster channel[11]. Each dielectric wall is divided into 10 cells with a length $\Delta r = h/10$. The time step is equal to 0.0195 s to warrant convergence. The MatLab software is employed to perform the numerical solving.

The adjective "semi-empirical" is used because for each studied element at the temperature T, the values of other elements' temperatures T_i are the ones recorded by means of infrared imaging. The advantage of this method is that it brings closer our model to the real thermal behaviour. In order to launch calculations the initial temperatures through the wall must be known. We will assume that at $t = 0$, the temperature through the wall is equal to the surface's temperature which is recorded by infrared imaging. Having a small initial gradient through the wall does not change much the results.

D. Fitted configuration factors

At that point, we are not yet able to numerically solve Eq. 14. Indeed, the magnitude of thermal radiation fluxes involved in the model depends on the grey body view factors, or configuration factors, G_i. These factors determine the flux ratio exchange between two grey and diffuse surfaces[6]. Contrarily to view factors F_i, they do not only depend on the geometry of the surfaces but also on their radiative properties. For two surfaces S_i and S_j, respectively at temperature T_i and T_j, the heat flux exchanged between i and j is:

- for a black body: $\phi_{i \rightarrow j} = F_{ij} \, \sigma \, (T_i^4 - T_j^4)$ (15)

- for a grey body: $\phi_{i \rightarrow j} = G_{ij} \, \sigma \, (T_i^4 - T_j^4)$, where $G_{ij} = \dfrac{1}{\dfrac{1-\varepsilon_i}{\varepsilon_i} + \dfrac{1}{F_{ij}} + \dfrac{1-\varepsilon_j}{\varepsilon_j} \dfrac{S_i}{S_j}}$.   (16)

Before calculating the G factor, we must first determine the view factors F. To do so, the thruster must be considered as an enclosure. The enclosure boundary is divided into areas so that over each of these areas the following restrictions are met:

- the temperature is uniform,
- the radiative parameters are independent of wavelength, direction and temperature,
- energy is emitted and reflected diffusely,
- the incident and hence reflected energy flux is uniform over each individual area.

The simplest enclosure is the one shown in Fig. 8. According to the precedent restrictions, each temperature field is uniform. Each part of the thruster was chosen according to the infrared imaging outcomes, which separate the discharge channel into three major areas: The external wall (1), the internal wall (2) and the bottom of the

Area	q_p (kW/m^2) "go and stop"	q_p (kW/m^2) model	P_{wall} (W) model	Input power (W)	Power losses (%)
Ext-front	6.4	3.5			
Ext-rear	2.6	1.5	97	1700	6
Int-front	4.7	6.5			
Ext-front	9.6	6.5			
Ext-rear	0.5	3	129	2100	6
Int-front	6.7	6			
Ext-front	10.9	6.5			
Ext-rear	0.3	4.5	136	2275	6
Int-front	6	5			
Ext-front	7.4	7.2			
Ext-rear	3.2	3.2	137	2400	6
Int-front	4.9	6.2			
Ext-front	14.9	14.5			
Ext-rear	1.3	4.4	201	3010	7
Int-front	7.1	6.2			
Ext-front	9.3	14			
Ext-rear	4	6.5	243	3200	8
Int-front	6.2	9			
Ext-front	24.9	21			
Ext-rear	5.5	9	321	4080	8
Int-front	8.6	9.5			
Ext-front	14.6	30			
Ext-rear	1.9	6	306	4290	7
Int-front	9.1	12			

Table 2. Power deposited by the plasma onto different parts of the outer and inner dielectric walls of a PPSX000 Hall thruster as a function of the applied power $I_d \times U_d$. The "go and stop" approach is compred to a full calculation.

channel (3) The enclosure is completed with the ejection face (0) which is considered at uniform temperature T_{env}. For such a simple enclosure shape, the view factors can be found in literature[12]. The theoretical values of the view factors are given in Table 1. The value of the grey body view factors can be determined from the theoretical F factors using formula 16 with $\varepsilon = 0.92$ for BN-SiO$_2$ and $\varepsilon = 0.8$ for the anode. The theoretical values of the grey body view factors are also given in Table 1.

There is still a factor which we have not yet determined: The heat flux lost by the outer dielectric wall through its external surface $\phi_{outside}$. One of the assumptions is that the environment is similar to a low-pressure medium at a constant temperature T_{env}. The heat loss can be seen as a simple heat exchange between two bodies at uniform temperature: The external wall at T and the environment at $T_{env} = 400$ K. Thus the heat flux radiated towards the outside writes:

$$\phi_{ext} = F_{ext}\, \sigma \left(T^4 - T_{env}^{\;4}\right) \approx F_{ext}\, \sigma\, T^4 , \tag{17}$$

where F_{ext} is the view factor between the outer wall and the surroundings. The energy conservation equation leads to $F_{ext} = \dfrac{A_{r+h}}{A_r} \approx 1.06$ for the PPSX000 thruster. A_r, respectively A_{r+h}, is the internal, respectively the external, area of the outer dielectric wall. To include the thruster environment in the model, the factor F_{ext} must be added to G_{11}. Of course, some of the components that surround the outer ceramic ring can exchange heat with the latter. We here
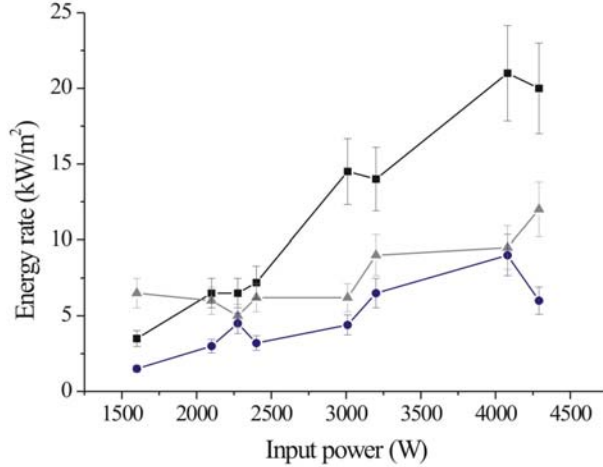
Figure 11. Power lost by the plasma onto the ceramic wall of the PPSX000 HET with a graphite anode as a function of the input power : $q_{\text{ext-front}}$ (square), $q_{\text{ext-rear}}$ (circle), $q_{\text{int-front}}$ (triangle). Error bars correspond to 15% of data.
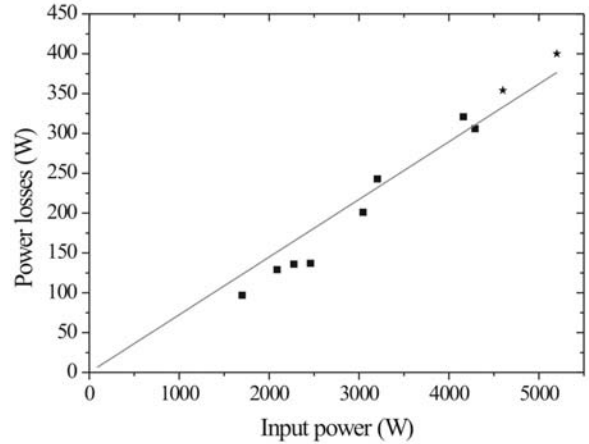
Figure 12. Power lost by the plasma onto the outer and inner dielectric wall of a PPSX000 thruster equipped with a graphite anode (square) and with a stainless steel anode (star). The solid lines correspond to a linear fit.

propose a first approach which does not take precisely into account the magnetic coils, the housing of the thruster and the vacuum chamber wall.

We must now compare the model outcomes to thermal imaging recordings to check the validity of all assumptions as well as to verify whether the calculation of the G factor based on a four sides rectangular enclosure permit to stick to reality. In order to avoid any mistake, the comparison must be carried out with a data set collected after a shutdown, i.e. without plasma. In such a way the term q_{p}, which is unknown, vanishes into equations. The result of the comparison can be seen in Fig. 9a. On the one hand, the graph shows that simulation does not image exactly the recorded temperature drop. On the other hand, the graph also shows that the simulated trend is in agreement with the observed one. There can be two reasons to explain the slight temperature difference between measurements and simulations. The first one is that the calculated G factors are not precise enough due to the simple radiative enclosure. The second reason is that there are probably nearby heat sources which introduce or retrieve heat from the system.

One way to be closer to the real HET thermal behavior is to slightly modify the value of G factors. This correction permits to account for possible "parasitic" heat exchanges which do not appear in our model. Data set recorded after thruster shutdowns are in fact used to fit G factors in such a way that measured and calculated temperature profiles do match each other. Figure 9b shows an example of fitting procedure outcome. To calculate G_{ij}, the average temperature $\overline{T}_j(t)$ of the surface j is used. The agreement between the two curves is very good. As can be verified in Table 1, the gap between theoretical and fitted G factors is rather low. Furthermore, for a given thruster configuration, the G factor values do not differ when using several data set.

The fitted factor method has another advantage. The number of theoretical G factors is directly linked with the chosen geometry: A four side enclosure was chosen to limit the complexity of G factor calculation. We can now choose to split the channel into as many parts as we want: To each area will correspond a series of fitted factors that can be determined experimentally. The energy conservation equation will always be in the form (for the sake of clarity heat conduction is neglected here):

$$\rho c_{\text{p}} h \frac{dT}{dt} = -(G_{11} + F_{\text{ext}})\,\sigma\,T_1^4(t) + G_{12}\,\sigma\,\overline{T}_2^{\,4}(t) + G_{13}\,\sigma\,\overline{T}_3^{\,4}(t) + \ldots + q_{\text{p}}, \tag{18}$$

where $\overline{T}$ refers to the mean area temperature.

V. Energy losses inside the channel of a PPSX000 Hall thruster

A. Determination of q_p

The time-dependent thermal model presented in previous chapter was used to determine the energy flux deposited by the plasma onto the inner and outer BN-SiO$_2$ walls of the PPSX000 thruster channel. The quantity q_p is the only unknown quantity in the model. It is then obtained by adjusting the calculated temperature profiles to the ones measured by means of calibrated infrared imaging. An example of numerical outcomes using fitted G factors is shown in Fig. 10 at 3.2 kW input power. As can be seen, the calculated evolution in time of the channel wall temperature is in good agreement with the measured one. The outer ceramic wall is divided into two areas: The rear half and the front half. The experimental configuration prevents from observing the rear half of the inner wall, as can be seen in Fig. 2. The temperature is assumed to be homogeneous over all areas. Also shown in Fig. 10 is the value of the power deposited by the plasma onto the dielectric walls.

All results are summarized in table 2. The "go and stop" approach can only be used directly for configurations preceded or followed by a shutdown. For the other configurations, the method still works but the slope difference gives the flux difference between the two configurations. A recursive treatment allows to determine all fluxes but errors propagate through the calculation. As already mentioned, the "go and stop" approach must be used to have a rough estimate of q_p. The use of the semi-empirical time-dependent model is then preferred. As shown in Table 2, the deposited power is always highest in the front half of the dielectric wall, which corresponds to the ionization-acceleration zone of the plasma. This fact is in favor of a power deposition mechanism that involves charged particles. The total power deposited onto dielectric wall P_{wall} is also indicated in Table 2. To perform the calculation we consider that the q_p ratio between the rear half and the front half is the same for the two walls. On the whole, P_{wall} is of about 7% of the input power.

In order to obtain the total amount of power lost by the plasma inside the channel, the anode and the rear dielectric part must be accounted for.

- for the anode, $P_{anode} = I_d \times E_s$, where E_s is the anode sheath potential drop (around 30 eV),

- we consider that the flux deposited by the plasma onto the rear ceramic is roughly the same as the one deposited onto the *Ext-rear* area: $P_{rear} = S_{rear} \times \phi_{ext\text{-}rear}$.

Finally, the total amount of power lost inside the channel is around 15% of the input power. The thrust efficiency of the PPSX000 Hall thruster is around 60% over the entire power domain. Thus some power loss mechanisms still remain to be identified and quantified. UV radiation escaping the channel is one possibility. Power can also be lost in the form of ion kinetic energy not converted into thrust (ion beam divergence).

B. Influence of the applied power

The power lost by the plasma onto the ceramic walls of the PPSX000 Hall thruster equipped with a graphite anode is plotted as a function of the input power in Fig. 11. The quantity q_p varies linearly with the input power for the 3 areas. In Fig. 11, one can observe that more power is bring onto the outer wall. The accuracy of estimation for the values of q_p was deduced from a statistical study of the model outcomes when shifting on purpose the temperature profiles and when changing the value of the G factors (thermodynamic properties were kept constant). We found that the accuracy is certainly better than 15%, which is the value used inf Fig. 11.

As can be seen in Fig. 12, the power deposited by the plasma onto the outer and inner dielectric discharge chamber walls of a PPSX000 thruster varies linearly with the input power:

$$P_{wall} = 0.072 \times P \tag{19}$$

P_{wall} is solely a function of the input power $P = I_d \times U_d$ meaning that it does not depends upon the current-voltage pair. Such a simple trend, already discussed in section III, is in contradiction with the complexity of the Hall thruster plasma dynamics.

VI. Conclusion

The semi-empirical time-dependent model of a Hall effect thruster we developed is well suited to extract the amount of energy deposited by the plasma onto the walls of the discharge chamber. In this contribution we presented the amount of power lost by the plasma onto the outer and inner walls of a PPSX000 thruster as a function of the applied power. In view of the results, two questions still remain:

- What is the origin of q_p? In other words, what is the energy losses mechanism? Are ions and electrons the only particles involved in the plasma-wall interaction processes?

- Why do P_{wall} and q_p vary linearly with the input power whatever the current-voltage pair?

To answer these questions will necessitate to carry out new series of measurement campaigns and to compare the experimental value of q_p with values calculated using a hybrid code.

Acknowledgments

References

[1] V. Kim, V. Kozlov, G. Popov, A. Skrylnikov, K. Kozubsky, M. Lyszyk, "Investigation of the stationary plasma thruster outgassing and its thermal state impact on thruster peformance variation in time", *Proceedings of the 26th International Electric Propulsion Conference*, Kitakyushu, Japan, paper 84, 1999, pp. 518-523.

[2] S. Roche, S. Barral, S. Béchu, M. Dudeck, P. Lasgorceix, L. Magne, T. Minea, D. Pagnon, M. Touzeau, "Thermal analysis of a stationary plasma thruster", *Proceedings of the 35th AIAA/ASME/SAE/ASEE Joint Propulsion Conference*, Los Angeles, AIAA paper 99-2296, 1999.

[3] M.W. Crofton, R.H. Uenten, L. Harris, E.M. Yohnsee, R.B. Cohen, "Calibrated infrared imaging for electric thrusters", *Proceedings of the 32nd AIAA/ASME/SAE/ASEE Joint Propulsion Conference*, Florida, AIAA paper 96-2977, 1996.

[4] S. Mazouffre, P. Echegut, F. Dubois, M. Dudeck, "Lessons learned from infrared thermal imaging of Hall effect thrusters", *Proceedings of the 4th International Spacecraft Propulsion Conference*, Sardina, Italy, ESA Proceedings SP-555, 26, 2004.

[5] O. Duchemin, P. Dumazert, N. Cornu, D. Estublier, F. Darnon, "Stretching the operational envelope of the PPS®X000 plasma thruster", *Proceedings of the 40th AIAA/ASME/SAE/ASEE Joint Propulsion Conference*, Fort Lauderdale, FL, AIAA paper 04-3605, 2004.

[6] R. Siegel and J.R. Howell, *Thermal Radiation Heat Transfer*, 2nd Ed., Taylor & Francis, Washington, 1972.

[7] ThermaCAM™ SC 3000 Operator's manual, FLIR systems AB, Publ. No. 557379, 1999.

[8] S. Mazouffre, P. Echegut, M. Dudeck, "A calibrated infrared imaging study on the steady state thermal behavior of Hall effect thrusters.", in preparation.

[9] V.V. Zhurin, H.R. Kaufman, R.S. Robinson, "Physics of closed drift thrusters", *Plasma Sources Sci. Technol.*, Vol. 8, 1999, pp. R1-R20.

[10] E.Y. Choueiri, "Plasma oscillations in Hall thrusters", *Phys. Plasmas*, Vol. 8, No. 4, 2001, pp. 1411-1426.

[11] J. Pérez Luna, "Time-resolved infrared thermal imaging: A means for the investigation of plasma-surface interactions in a Hall effect thruster", Laboratoire d'Aérothermique, Internal Report No. 2005-08, 2005.

[12] J.R. Howell, *A catalogue of Radiation heat transfer configuration factors*, University of Texas at Austin, http://www.me.utexas.edu/~howell/tablecon.html